HAL open science

The Dynamics of the West African Monsoon. Part V: The Detection and Role of the Dominant Modes of Convectively Coupled Equatorial Rossby Waves

Serge Janicot, Flore Mounier, Sébastien Gervois, Benjamin Sultan, George N. Kiladis

▶ **To cite this version:**

Serge Janicot, Flore Mounier, Sébastien Gervois, Benjamin Sultan, George N. Kiladis. The Dynamics of the West African Monsoon. Part V: The Detection and Role of the Dominant Modes of Convectively Coupled Equatorial Rossby Waves. Journal of Climate, 2010, 23, pp.4005-4024. 10.1175/2010JCLI3221.1 . hal-00758832

HAL Id: hal-00758832

https://hal.science/hal-00758832v1

Submitted on 2 Nov 2021

HAL is a multi-disciplinary open access archive for the deposit and dissemination of scientific research documents, whether they are published or not. The documents may come from teaching and research institutions in France or abroad, or from public or private research centers.

L'archive ouverte pluridisciplinaire **HAL**, est destinée au dépôt et à la diffusion de documents scientifiques de niveau recherche, publiés ou non, émanant des établissements d'enseignement et de recherche français ou étrangers, des laboratoires publics ou privés.

Distributed under a Creative Commons Attribution 4.0 International License

The Dynamics of the West African Monsoon. Part V: The Detection and Role of the Dominant Modes of Convectively Coupled Equatorial Rossby Waves

SERGE JANICOT

LOCEAN/IPSL, IRD, UPMC, Paris, France

FLORE MOUNIER

EQECAT, Paris, France

SÉBASTIEN GERVOIS

LATMOS/IPSL, CNRS, UPMC, Paris, France

BENJAMIN SULTAN

LOCEAN/IPSL, IRD, UPMC, Paris, France

GEORGE N. KILADIS

NOAA/ESRL/Physical Sciences Division, Boulder, Colorado

(Manuscript received 24 April 2009, in final form 3 March 2010)

ABSTRACT

This study is the last in a series of papers addressing the dynamics of the West African summer monsoon at intraseasonal time scales between 10 and 90 days. The signals of convectively coupled equatorial Rossby (ER) waves within the summer African monsoon have been investigated after filtering NOAA outgoing longwave radiation (OLR) data within a box delineated by the dispersion curves of the theoretical ER waves. Two families of waves have been detected in the 10–100-day periodicity band by performing a singular spectrum analysis on a regional index of ER-filtered OLR. For each family the first EOF mode has been retained to focus on the main convective variability signal.

Within the periodicity band of 30–100 days, an ER wave pattern with an approximate wavelength of 13 500 km has been depicted. This ER wave links the MJO mode in the Indian monsoon sector with the main mode of convective variability over West and central Africa. This confirms the investigations carried out in previous studies.

Within the 10–30-day periodicity band, a separate ER wave pattern has been highlighted in the African monsoon system with an approximate wavelength of 7500 km, a phase speed of 6 m s^{-1}, and a period of 15 days. The combined OLR and atmospheric circulation pattern looks like a combination of ER wave solutions with meridional wavenumbers of 1 and 2. Its vertical baroclinic profile suggests that this wave is forced by the deep convective heating. Its initiation in terms of OLR modulation is detected north of Lake Victoria, extending northward and then propagating westward along the Sahel latitudes.

The Sahel mode identified in previous studies corresponds to the second main mode of convective variability within the 10–30-day periodicity band, and this has also been examined. Its pattern and evolution look like the first-mode ER wave pattern and they are temporally correlated with a coefficient of +0.6. About one-third of the Sahel mode events are concomitant with an ER wave occurrence. The main difference between these two signals consists of a stronger OLR and circulation modulation of the Sahel mode over East and central Africa. Thus, the Sahel mode occurrence and its westward propagation could be explained in part by atmospheric dynamics associated with the ER waves and in part by land surface interactions, as shown in other studies.

Corresponding author address: Dr. Serge Janicot, Boite 100, 4 Place Jussieu, LOCEAN/IPSL, Université Pierre et Marie Curie, 75252 Paris CEDEX 05, France.
E-mail: serge.janicot@locean-ipsl.upmc.fr

DOI: 10.1175/2010JCLI3221.1

© 2010 American Meteorological Society

Unauthenticated | Downloaded 11/02/21 07:41 PM UTC

1. Introduction

This paper is the last in a series of studies documenting the West African summer monsoon variability at intraseasonal time scales (Sultan and Janicot 2000; Janicot and Sultan 2001; Sultan et al. 2003; Sultan and Janicot 2003; Mounier and Janicot 2004; Mounier et al. 2008; Janicot et al. 2009; Sultan et al. 2009). In this region the intraseasonal time scale is critical for agriculture and livestock farming, which are strongly rainfall dependent. A dry spell occurring during a critical stage of the crop development can induce a bad yield even if the total season rainfall amount is good (Sultan et al. 2005). However, the basic mechanisms controlling this variability are largely unknown and its known predictability is very weak, even while higher-frequency weather and lower-frequency seasonal forecasts do have some skill.

Within the intraseasonal scale, two main periodicities have been highlighted. The first is between 10 and 25 days, and is rather recurrent along the summer monsoon season, and the second is between 25 and 90 days, and is more intermittent (Janicot and Sultan 2001). At the 10–25-day range two modes have been identified over West and central Africa through a spatial EOF (S-EOF; Richman 1986) analysis on convection fields (Mounier and Janicot 2004). One mode is primarily characterized by a quasi-stationary zonal dipole of convection within the intertropical convergence zone (ITCZ), with its two poles centered along the Guinean coast and on 30°–60°W in the equatorial Atlantic, and a modulation of the zonal low-level wind between these poles [the quasi-biweekly zonal dipole mode (QBZD); see Mounier et al. 2008]. This mode appears to be controlled both by equatorial atmospheric dynamics through a Kelvin wave–like disturbance propagating eastward between its two poles, and by land surface processes over Africa, which induces combined fluctuations in surface temperatures, surface pressure, and low-level zonal winds off the coast of West Africa.

The second mode, called in the following the ''Sahel'' mode, is a westward-propagating signal from eastern Africa to the tropical Atlantic, with increased cyclonic circulation being located ahead of an enhanced convective envelope. This signal is consistent with a signal previously detected over the Sahel based on a regional rainfall index (Sultan et al. 2003). Taylor (2008) showed that land–atmosphere interaction processes can contribute to the maintenance and westward propagation of the Sahel mode. Extensive areas of wet soil associated with the positive phase of the Sahel mode induce weak surface sensible heat fluxes and a low-level anticyclonic circulation, which brings moisture ahead of the convective zone and helps promote its westward propagation. However, GCM simulations carried out with and without intraseasonal land surface couplings suggest that this westward-propagating mode is mainly controlled by a purely internal atmospheric mode (Lavender et al. 2010).

On the global scale Matthews (2004) showed that the remote circulation of the Madden–Julian oscillation (MJO; Madden and Julian 1994) over the warm pool sector offers a plausible explanation for the dominant mode of variability in convection over West and central Africa at the 20–200-day time scales. Twenty days prior to an enhancement of convection over Africa, MJO convection is decreasing over the equatorial warm pool. In response to this change in warm pool convection, a dry equatorial Kelvin wave propagates eastward, a dry equatorial Rossby (ER) wave response propagates westward, and between them they complete a circuit of the equator and meet up 20 days later over Africa, favoring an enhancement of deep convection. Matthews' results were confirmed by Maloney and Shaman (2008), who, using Tropical Rainfall Measuring Mission (TRMM) precipitation, showed that the MJO explains about 30% of 30–90-day precipitation variance in the West African monsoon region. Janicot et al. (2009) and Pohl et al. (2009) further investigated the 25–90-day variability of convection in the African monsoon. They showed that the dominant mode highlighted by Matthews over West and central Africa is not completely stationary but is characterized by a westward propagation of the OLR anomalies in its northern part. These convectively coupled ER and MJO signals appear to contribute significantly to the evolution of this mode, while the convectively coupled Kelvin wave shows a very weak impact. Recently, Lavender and Matthews (2009) supported Matthews' results through atmospheric general circulation model simulations mimicking the MJO-like convection over the warm pool, and they also confirmed the primary role of the convectively coupled ER wave.

However, there is more to the global control of the African summer monsoon than equatorial dynamics. The active–break cycle of the Indian monsoon, controlled by a northward-moving dipole of diabatic heating in the Indian sector, also influences the African monsoon through atmospheric teleconnections (Janicot et al. 2009). This influence is transferred through the northern Indian heat source. This excites a Gill-type Rossby cyclonic circulation propagating westward over North Africa after it cuts off due to the northward arrival of the equatorial Indian heat source and the associated intrusion of an anticyclonic ridge. Low-level westerly winds and moisture advection within the ITCZ consequently increase over Africa. The mean time lag between an active phase over India and over Africa is about 15–20 days.

Unauthenticated | Downloaded 11/02/21 07:41 PM UTC

In this paper we investigate the role of the convectively coupled ER waves in the African monsoon more precisely, using the detection technique developed by Wheeler and Kiladis (1999) and already applied over Africa in Kiladis et al. (2006), Mounier et al. (2007, 2008), and Janicot et al. (2009). The datasets are detailed in section 2. In section 3 a spectral analysis of the ER signal over Africa is performed, which distinguishes two periodicity bands: one between 10 and 30 days and one between 30 and 100 days. The dominant mode of the 30–100-day ER signal is analyzed in section 4, and its connection with the main African mode highlighted by Matthews (2004) and Janicot et al. (2009) is confirmed. In section 5 the dominant mode of the 10–30-day ER signal is examined and compared with the patterns and occurrences of the Sahel mode detected by Sultan et al. (2003) and Mounier and Janicot (2004). Its potential role in the internal atmospheric mode highlighted by Lavender et al. (2010) is addressed. Conclusions are given in section 6 and a short synthesis of this series of studies documenting the intraseasonal variability in the African summer monsoon is added. Note that the term ''mode'' is used in reference to the S-EOF process, which has been used to extract these signals.

2. Datasets

a. The NCEP/DOE AMIP-II Reanalysis

The National Centers for Environmental Prediction–National Center for Atmospheric Research (NCEP–NCAR) reanalysis dataset (Kalnay et al. 1996) provides a gridded analysis of the global observational network of meteorological variables (wind, temperature, geopotential height, humidity on pressure levels, surface variables) and flux variables, such as precipitation rate and radiative and turbulent fluxes. The reanalysis uses a ''frozen'' state-of-the-art analysis and forecast system at a triangular spectral truncation of T62 to perform data assimilation throughout the period from 1948 to the present. Data are reported on a 2.5° × 2.5° grid every 6 h (0000, 0600, 1200, and 1800 UTC) on 17 pressure levels from 1000 to 10 hPa, as well as the surface level, which are adequate resolutions for studying synoptic weather systems. The NCEP/Department of Energy (DOE) Atmospheric Model Intercomparison Project (AMIP)-II Reanalysis (R-2) dataset, the updated version of the NCEP–NCAR reanalysis, has been used here over the period of 1979–2006 with one value per day by averaging the four outputs of each day. This version of the reanalysis shows significant improvements over the original, especially for land surface parameters and surface–air fluxes (Kanamitsu et al. 2002).

b. The NOAA OLR dataset

Since 1974, polar-orbiting National Oceanic and Atmospheric Administration (NOAA) Television and Infrared Observation Satellite (TIROS) satellites have established a quasi-complete series of twice-daily outgoing longwave radiation (OLR) at the top of the atmosphere at a resolution of 2.5° latitude–longitude (Grueber and Krueger 1974). The daily-interpolated OLR dataset produced by the Climate Diagnostic Center (Liebmann and Smith 1996) has been used here over the period of 1979–2006 as a proxy for deep convection. Local hours of the measurements varied during the period of 1979–90 between 0230 and 0730 UTC in the morning and between 1430 and 1930 UTC in the afternoon. Because deep convection over West Africa has a strong diurnal cycle, a sample of daily OLR based on two values separated by 12 h is obtained to get a daily average. Wheeler et al. (2000), Straub and Kiladis (2002), and Roundy and Frank (2004), among others, have illustrated the utility of OLR in tracing convectively coupled equatorial waves.

c. The IRD daily rainfall dataset

To validate the OLR data, a daily interpolated in situ rainfall dataset available from the Institut de Recherches pour le Développement (IRD) has been used. Daily rainfall amounts at stations located within the West African domain of 3°–20°N, 18°W–25°E have been compiled. These data are available for the period of 1968–90, utilizing more than 1300 stations from 1968 to 1980, and between 700 and 860 for the period of 1981–90. These daily values were interpolated to the same 2.5° × 2.5° grid as NOAA OLR and NCEP fields, by assigning each station daily value to the nearest grid point and averaging all of the values related to each grid point. The greatest density of stations is located between the latitudes of 5° and 15°N. Data along 17.5°N can also be taken into account because 30–45 stations are available near that latitude.

d. The GPCP daily rainfall dataset

Finally, the Global Precipitation Climatology Project (GPCP) One-Degree Daily (1DD) combination was used over the available period of 1997–2006 to complement the results obtained with the other datasets. This rainfall estimate product is based on 3-hourly merged global infrared brightness temperature histograms on a 1° × 1° grid in the 40°N–40°S band (Huffman et al. 2001). It has the advantage of providing global coverage, unlike the IRD rainfall dataset, and of having a better sampling than the NOAA OLR dataset. On the other hand, because it is only available since 1997, it can be used only as a complement to the NOAA OLR data to carry out our

Unauthenticated | Downloaded 11/02/21 07:41 PM UTC

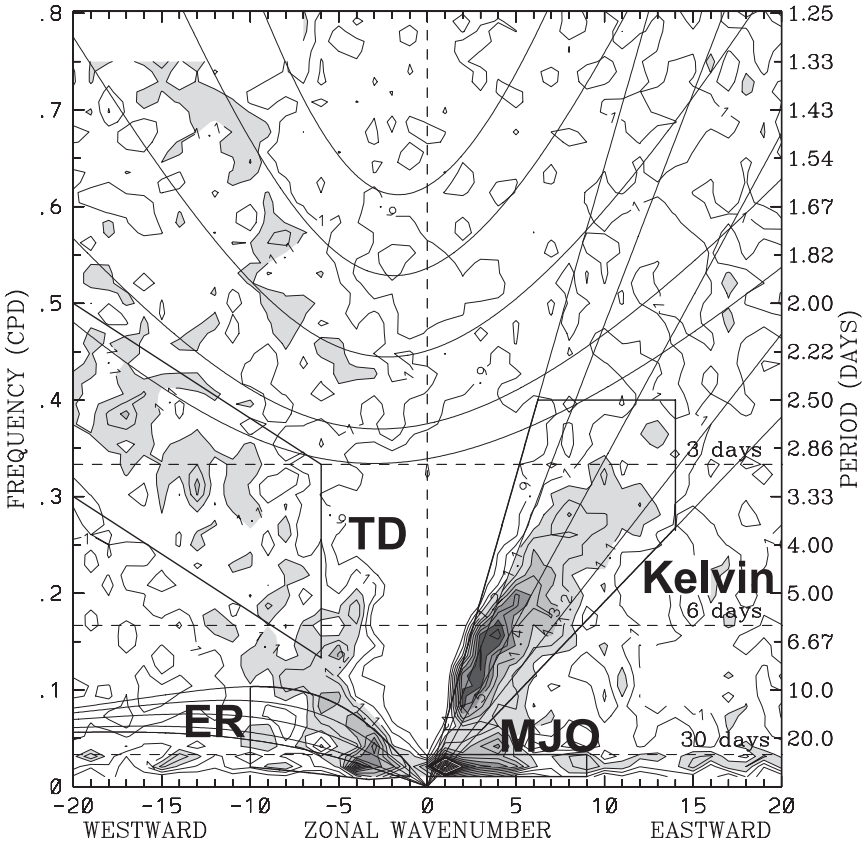

FIG. 1. Regions of wavenumber–frequency filtering calculated for June–September 1979–2006. Contours show the symmetric OLR power divided by a background spectrum [note that the background was calculated for the full 22 yr; see Wheeler and Kiladis (1999) for details on the computation techniques]. Contour interval of this ratio is 0.1, starting at 0.9, with shading above 1.1 indicating statistically significant signals. The regions of the wavenumber–frequency domain used for filtering of the OLR dataset to retrieve the longitude–time information of these convectively coupled equatorial waves (Kelvin, TD, ER, and MJO) are indicated (thick boxes). The various equatorial wave dispersion curves for the five different equivalent depths of h = 8, 12, 25, 50, and 90 m are shown (thin lines).

investigation; for instance, it will not be used in section 4 (the 30–100-day signal) because the number of cases available over the period of 1997–2006 to compute composite fields is too small (18 and 13 for high and weak rainfall amounts, respectively; see Table 3). Moreover, because it is based on infrared histograms, its rainfall estimate may have large errors when rainfall is produced by warm-top clouds.

3. Detection of the equatorial Rossby signals over West Africa

a. The detection of convectively coupled signals

Figure 1 shows a wavenumber–frequency spectral analysis of the OLR component symmetric about the equator between 15°N and 15°S for June–September 1979–2006. The shaded spectral peaks lie above the 95% level of significance, and a family of equivalent depth curves for Kelvin, ER, and inertial-gravity waves from equatorial linear shallow-water theory (Matsuno 1966) are also shown (see Wheeler and Kiladis 1999 for more details). The spectrum reveals the existence of two peaks corresponding to Kelvin and ER waves, lying along equivalent depth curves of around 20–50 m. For the Kelvin wave, this corresponds to an eastward phase speed of around 15 m s^{-1}. The MJO peak is also visible in the spectrum but does not correspond to a shallow-water mode. In Wheeler and Kiladis (1999) and Kiladis et al. (2006), a so-called tropical depression (TD) band representing easterly waves in Africa was also identified during northern summer in the westward-propagating signal domain for 2–6-day periods and 6–20 westward zonal wavenumbers. The boxes outline the regions of

Unauthenticated | Downloaded 11/02/21 07:41 PM UTC

filtering for all of these signals. This filtering has been performed for the ER signal by creating an OLR dataset through an inverse transform, which only retains the Fourier coefficients within the corresponding ER box in Fig. 1. Note that the dataset obtained contains the ER as well as a significant amount of background convection.

The dispersion curves in Fig. 1 assume a zero wind background state. However, it has been shown that the theoretical ER waves structures are very sensitive to a nonzero basic zonal flow with or without a meridional shear, resulting from Doppler and non-Doppler effects (Zhang and Webster 1989; Yang et al. 2003). For instance, assuming an easterly background state for the steering level of ER waves over West Africa, the dispersion curves asymptote to the left to a line extending upward to the left from the origin that represents the background wind speed. Thus, as wavenumber increases, the ER wave signal would merge with and become indistinguishable from the TD signature. However, at this point there is no theoretical or empirical basis to justify expanding or contracting the ER filter to some arbitrary cutoffs based on Fig. 1. Moreover, this would not result in substantially different patterns than what is presented further. The filter used here was designed to be consistent with Kiladis et al. (2009), and is an expanded version of the original used by Wheeler and Kiladis (1999), which now extends down to 1-m equivalent depth in order to account for the large region of variance at periods of greater than 40 days. Because the total OLR spectrum is very red, with much more power down at the lowest wavenumbers and frequencies, the filter already contains the bulk of the variance associated with the ER wave.

b. *The SSA analysis of the ER signal over West Africa*

The first step in the ER signal analysis over West Africa is to perform a singular spectrum analysis (SSA) on an "ITCZ index" of ER-filtered OLR values in order to identify its main periodicities. The ITCZ index represents the average of the daily OLR values over the 7.5°–12.5°N, 10°W–10°E domain, which is the mean summer location of the ITCZ over West Africa. SSA (Vautard and Ghil 1989; Vautard et al. 1992; Ghil et al. 2002) is related to EOF analysis but is applied to a lagged time series providing SSA modes that correspond to oscillations in a specific frequency band. Given the time series of the ER-filtered ITCZ index as $x(t)$ of length N, x is embedded in a vector space of dimension M to represent the behavior of the system by a succession of overlapping views of the series through a sliding M-point window. SSA provides eigenvectors, the EOFs in the time domain (T-EOFs), and quasi-periodic modes appear as pairs of degenerate eigenvalues associated with T-EOFs in quadrature. The projection of the original time series onto the kth T-EOF gives the corresponding principal components in the time domain (T-PCs). One can reconstruct the part of the original time series associated with the mode k, RC_k, by combining the kth T-EOF and the kth T-PC. The RCs are additive and the original time series can be reconstructed by summing up the M reconstructed components RC_k. As done in Sultan et al. (2009), a value of 50 has been used for M. Similar analyses have been performed for different values of M (40 and 60), and the results were not very sensitive to these different window sizes.

The results of the SSA applied on the ER-filtered ITCZ index are presented in Table 1 and Fig. 2. Table 1 shows the explained variance of the first 10 T-EOFs. Most of the variance is explained by these 10 components (98.5%), and 80% is explained by only the first six components, which have been retained here. Oscillatory modes can be detected by pairs of eigenvalues that are approximately equal and by T-EOFs in quadrature (see left side of Fig. 2). Figure 2 also displays on the right the maximum entropy method (MEM) spectrum of the total ER-filtered ITCZ index (in blue) and of the reconstructed signal by pairs of components (RC_{1-2}, RC_{3-4}, and RC_{5-6}) in red. The spectrum of the total ER-filtered ITCZ index has two ranges of high energy (and higher than the 95% significance level), between 12 and 50, and between 50 and 95 days. The first oscillatory mode is captured by the first pair of T-EOFs in quadrature, representing 34% of the variance. It is characterized by a periodicity band between 30 and 100 days (higher than the 95% significance level) with high energy between 40 and 70 days and a spectral peak between 50 and 60 days. The following pair of T-EOFs represents another oscillatory mode (26% of the variance) with high energy between 20 and 30 days and a spectral peak around 25 days. The third pair of T-EOFs extracts a weaker oscillatory mode (20% of variance) with high energy between 13 and 20 days and a spectral peak at 18 days.

The SSA is well designed to extract periodic information from noisy time series. Sultan et al. (2009) applied a similar SSA but on an unfiltered ITCZ index and they compared to the results obtained from an S-EOF analysis, which identified the "QBZD," "Sahel," and "MJO" modes as described in the introduction. They showed that the first SSA mode is highly correlated to the MJO mode, and that the combination of the second and third SSA modes is highly correlated to the combination of the QBZD and the Sahel modes. There is not a unique correspondence between the individual second and third SSA modes and the QBZD and the Sahel modes because the SSA aims at separating the

Unauthenticated | Downloaded 11/02/21 07:41 PM UTC

TABLE 1. Percentages of explained variance of the first 10 T-EOFs.

Eigenvalue	Variance (%)	Cumulated variance (%)
1	17.1	17.1
2	16.9	34.1
3	13.8	47.9
4	12.2	60.1
5	10.4	70.5
6	9.4	79.8
7	6.7	86.6
8	5.5	92.1
9	3.6	95.7
10	2.8	98.5

periodicities while the S-EOF aims at differentiating the spatial structures. Because the QBZD and the Sahel modes have close periodicities, they cannot be differentiated by SSA. With regard to the results presented here, we have chosen to separate the ER signal into only two periodicity bands, one between 10 and 30 days, and one between 30 and 100 days. The ER-filtered OLR values have then been filtered within these two periodicity bands separately, and for each of them the main S-EOF mode has been extracted and they are examined in the next sections.

4. Analysis of the primary 30–100-day ER mode

a. *The S-EOF patterns*

A S-EOF analysis has been performed on the 30–100-day filtered ER OLR signal over West and central Africa (10°S–30°N, 80°W–60°E) on June–September 1979–2006. To determine the number of PCs to be retained, the Scree test (Cattell 1966) and the North et al. (1982) rule of thumb were used. Following these constraints, PC1–PC2 form an ''effectively degenerate multiplet'' that is very well separated from PC3. PC1 and PC2 represent, respectively, 16.6% and 14.9% of the filtered variance, for a total of 31.5% (Table 2). This enables us to focus on the main mode of the 30–100-day ER wave and remove some background signal retained in the

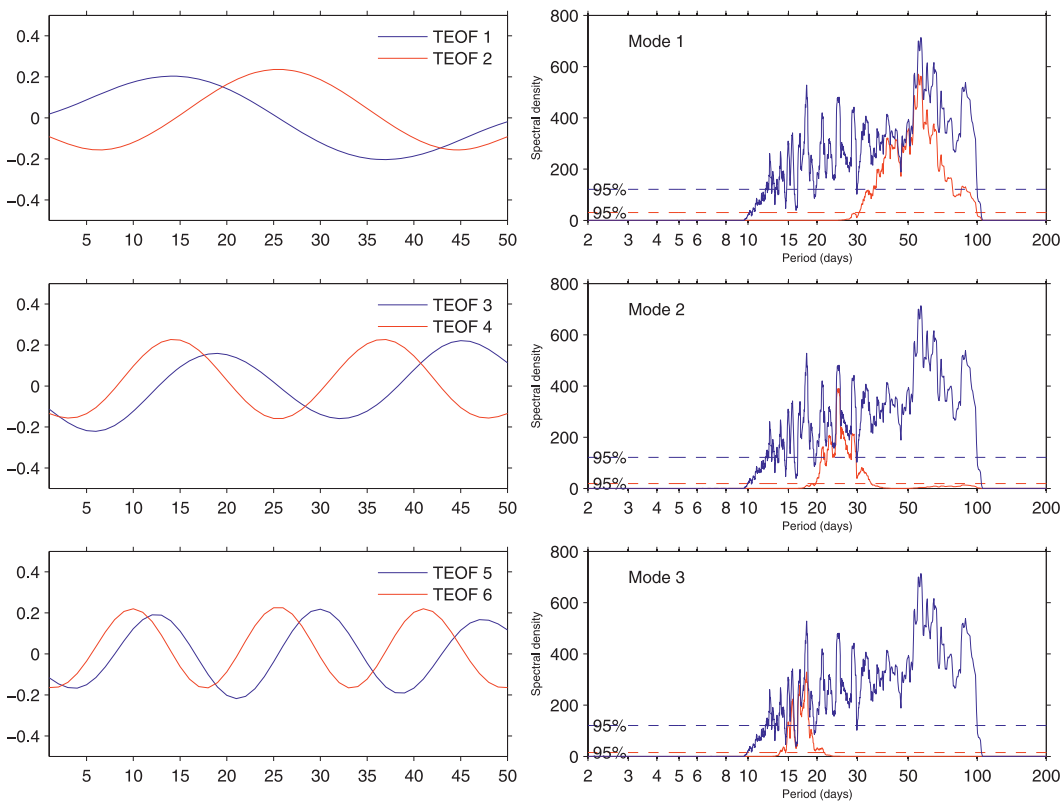

FIG. 2. (left) Pairs of the T-EOFs corresponding to the three intraseasonal modes captured by the SSA. (right) The MEM spectrum of the ER-filtered ITCZ index (blue lines) and for each intraseasonal mode (red lines): Modes (top) 1, (middle) 2, and (bottom) 3. The SSA–MEM spectrum has been applied separately to the sum RC_{1-2}, RC_{3-4} and RC_{5-6}. The order of the MEM spectrum is 50 days. The 95% significance levels are displayed (dashed horizontal lines).

Unauthenticated | Downloaded 11/02/21 07:41 PM UTC

TABLE 2. Percentages of explained variance of the S-EOF of the 30–100-day filtered ER signal.

Eigenvalue	Variance (%)	Cumulated variance (%)
1	16.6	16.6
2	14.9	31.5
3	8.9	40.4
4	7.2	47.6
5	6.2	53.8
6	5.3	59.1

filtering procedure. Figure 3 (top) shows the two first eigenvectors that are in spatial quadrature and depicts an approximate half-wavelength of 55° of longitude, or about 12 000 km for the whole wavelength. Figure 3 (middle) shows the composite field of total ER OLR (contours) for the difference between the strong and the weak convective phase. This has been computed by reconstructing ER OLR values over the ITCZ area 7.5°–12.5°N, 10°W–10°E using combined S-EOF1 and S-EOF2 reconstruction (''S-EOF12''). We focus on the strong cases, but the reverse pattern is obtained for the weak cases. We designate a strong phase as an ER wave occurrence over West and central Africa when the reconstructed S-EOF12 ITCZ index is negative, meaning stronger convective activity in the ITCZ. The strong cases have been selected when the standardized reconstructed ITCZ index is minimum and less than minus one. Similar composite fields for unfiltered rainfall data are also displayed (color) over the period of 1979–90 where rainfall data are available. This yields an average of 1.5 strong and 1.8 weak cases per summer (Table 3). Negative OLR anomalies are centered at around 0°W, and weak positive OLR poles are located around 60°E and between 100° and 45°W. This forms a more or less asymmetrical pattern with a mean wavelength of 13 500 km, which is a bit longer than the one estimated from the EOF patterns. The positive unfiltered rainfall anomalies seen over West and central Africa where data are available correspond rather well with the negative OLR values. The high range of these OLR and rainfall differences between the strong and weak phases means that these waves, while infrequent, are able to significantly modulate the convective activity over most of West and central Africa during the summer monsoon. Figure 3 (bottom) shows as an illustration the PC1 and PC2 time series in summer 1979. This depicts a similar contribution to these two components with weaker weights during the first half of June. These components are in temporal quadrature and have a periodicity between 40 and 45 days. We will see in the following that this is associated with a westward-propagating signal, consistent with the identification of ER waves.

b. The composite fields on the global tropics

Figure 4 presents the time sequence of strong minus weak convective events for June–September 1979–2006. It is based on the 30–100-day filtered ER OLR ITCZ index reconstructed by S-EOF12 in terms of unfiltered OLR values and 925-hPa geopotential heights. This sequence goes from $t_0 - 21$ to $t_0 + 9$ days with a 3-day lag, where t_0 is the reference day for the selected cases as in Fig. 3. The pattern at t_0 on Fig. 4 shows an enhancement of convection (negative OLR values) over most of West and central Africa. This spatial pattern is centered on the climatological mean of the ITCZ OLR field (in summer the ITCZ is located along 10°N), resulting in a modulation of convective activity within the ITCZ without any significant changes in its latitudinal location. The time sequence highlights a clear westward extension of the OLR anomalies, with negative OLR anomalies beginning to appear north of Ethiopia at $t_0 - 18$. They grow and extend westward up to t_0, and dissipate after t_0 when they reach the Atlantic. The dominant westward-propagating signal seen in the unfiltered OLR fields, as well as OLR anomalies, has an amplitude of more than 15 W m^{-2}, consistent with the detection of an ER response as an important factor in West African monsoon (WAM) variability at these time scales.

In addition to the evolution of the dominant ER mode of convection over Africa seen on Fig. 4, a large MJO-type signal is evident over the Indian–west Pacific sector. This consists of a meridional dipole of convection moving northward. At $t_0 - 18$ a positive OLR anomaly pole is located at the equator while convection is enhanced over India, corresponding to an active phase in the Indian monsoon. The equatorial positive OLR anomaly grows and reaches India at $t_0 - 12$, consistent with the occurrence of a break in the Indian monsoon up to $t_0 + 6$. Then, an active phase begins with the northward propagation of the following negative OLR anomaly. The associated atmospheric patterns in Fig. 4 combine as follows: 1) an ER wave characterized by a horseshoe-shaped pattern symmetric about the equator with positive geopotential height anomalies developing westward at $t_0 - 10/t_0$; and 2) a Gill-type Rossby cyclonic circulation excited by the northern Indian heat source and propagating westward over North Africa.

This field's evolution on Fig. 4 is very similar to the one presented in Fig. 2 of Janicot et al. (2009), which describes the sequence of the dominant 25–90-day S-EOF mode over Africa (except that filtered OLR is presented in their Fig. 2 while unfiltered OLR is presented here, leading to more noise). This S-EOF was based on just 25–90-day filtering, not ER space–time filtering. Therefore, the main 25–90-day signal identified over Africa

Unauthenticated | Downloaded 11/02/21 07:41 PM UTC

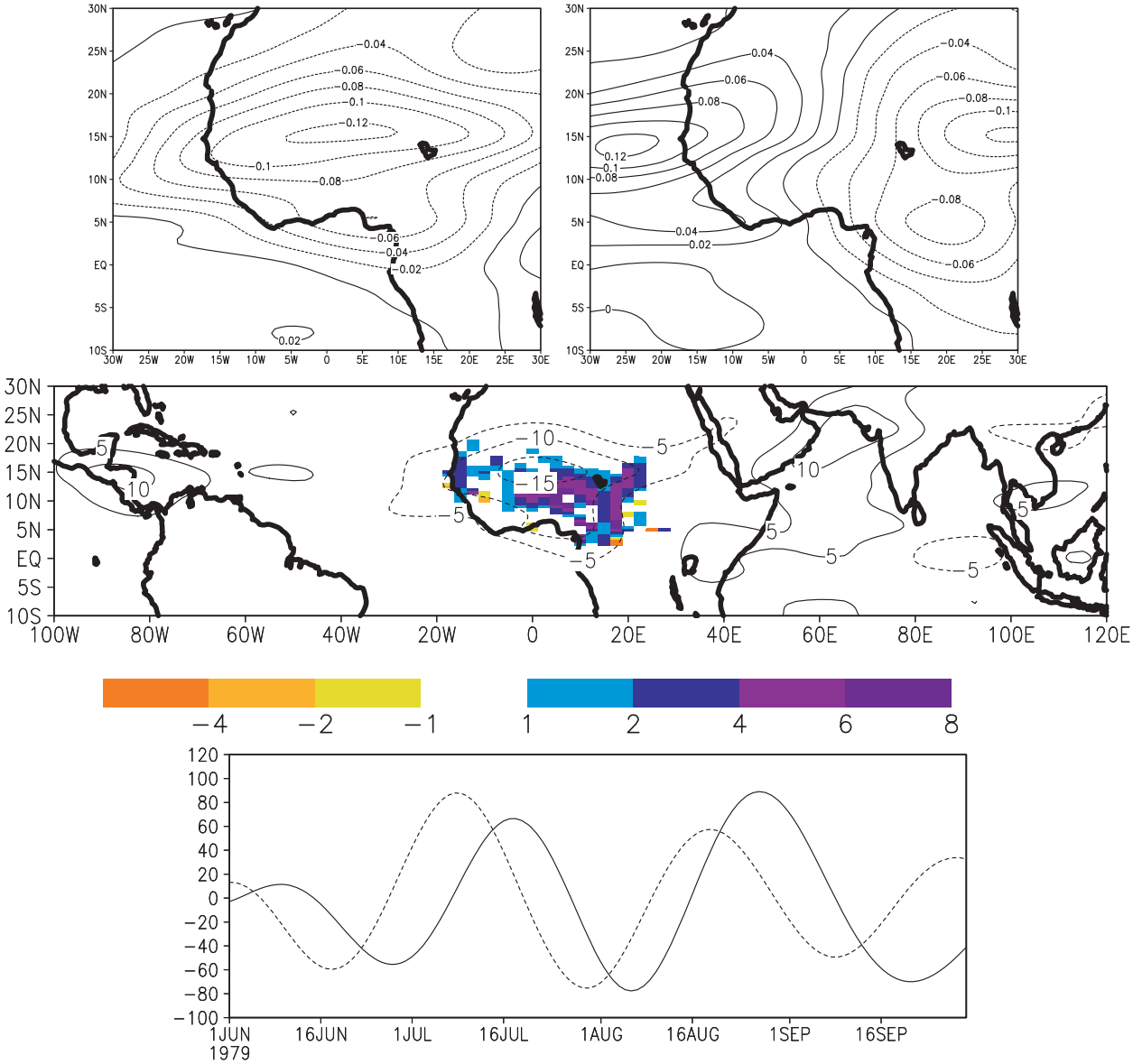

FIG. 3. (top) June–September 1979–2006 (left) first and (right) second eigenvectors of the S-EOF analysis of the 30–100-day filtered ER OLR signal over West and central Africa. (middle) Composite fields of the total ER-filtered OLR (contours) for the difference between strong and weak convective phase, computed by using the reconstruction of the OLR values over the ITCZ area 7.5°–12.5°N, 10°W–10°E by S-EOF12. The strong (weak) cases have been selected when the standardized reconstructed OLR ITCZ index is minimum (maximum) and weaker (higher) than minus (plus) one. Similar composite fields for unfiltered rainfall data, but over the period 1979–1990 (colors). OLR difference units: W m^{-2} and rainfall difference units: mm day^{-1}. (bottom) Time series of PC1 (solid line) and PC2 (dashed line) for the 1979 summer.

can indeed be attributed to the ER portion of the spectrum and not to the eastward-propagating MJO portion. The MJO-like pattern that is present over the Indian–west Pacific sector on Fig. 4, based on unfiltered OLR, but not present in the ER-filtered pattern on Fig. 3, means that ER and MJO are concomitant but they constitute different phenomena. This confirms that a convectively coupled ER signal within the 30–100-day periodicity band is a major driver in the MJO–WAM connection.

5. Analysis of the primary 10–30-day ER mode and comparison with the Sahel mode

Taylor (2008) and Lavender et al. (2010) showed that land–atmosphere interaction processes can contribute to the maintenance and the westward propagation of the Sahel mode, but they concluded that this westward propagation is mainly controlled by a purely internal atmospheric mode. The objective in this section is twofold:

Unauthenticated | Downloaded 11/02/21 07:41 PM UTC

TABLE 3. Number of cases selected for the composite datasets over June–September 1979–2006. The threshold of ±one standard deviation is used on the corresponding PCs. When using the GPCP dataset, the samples are weaker because of the shorter period of the dataset 1997–2006.

Filtered ER signal	Weak OLR	Strong OLR	Weak GPCP	Strong GPCP
EOF12 (30–100-day)	50	41	13	18
EOF12 (10–30-day)	118	117	39	43
EOF234 (10–30-day)	125	121	45	44

first to characterize the primary 10–30-day ER mode, and second to see if this ER mode can contribute to the westward propagation of the Sahel mode.

a. The 10–30-day ER mode

1) THE S-EOF PATTERNS

A similar S-EOF analysis has been performed on the 10–30-day filtered ER OLR signal over West and central Africa during summer. PC1–PC2 also form an ''effectively degenerate multiplet'' that is well separated from PC3. PC1 and PC2 represent, respectively, 15.5% and 13.7% of the filtered variance, that is, a total of 29.2% (Table 4). Figure 5 (top) shows the two first eigenvectors, which are in spatial quadrature. Figure 5 (middle) shows the associated composite field of total ER OLR (contours) for the difference between the strong and wet convective phase based on these two first EOF. In Fig. 3, this has been computed by reconstructing ER OLR values over the ITCZ area 7.5°–12.5°N, 10°W–10°E using combined S-EOF1 and S-EOF2 reconstruction. As previously done, the strong cases have been selected when the standardized reconstructed ITCZ index is minimum and less than −1. The reverse has been done for the weak cases. Similar composite fields for unfiltered rainfall data are also displayed (color). This yields an average of 4.2 strong and 4.2 weak cases per summer (Table 3). Negative OLR anomalies are centered at around 0°W and positive OLR poles are located around 30°E and 35°W, giving a mean wavelength of 7000 km. The positive rainfall anomalies seen over West and central Africa where data are available correspond rather well with the negative OLR values, except that rainfall anomalies extend more eastward than OLR anomalies. This discrepancy can be partly explained by the fact that we compare filtered with unfiltered data. [Figure 7a shows the corresponding composite unfiltered OLR field and Fig. 7b shows the corresponding composite unfiltered GPCP field. The negative OLR values extend more to the east than the filtered ones (the -5 W m^{-2} isoline is located west of Lake Chad for filtered data and east of Lake Chad for the unfiltered data), consistent with unfiltered positive GPCP and IRD rainfall values.] The high range of these OLR and rainfall differences between the strong and weak phases means that these waves are able to significantly modulate the convective activity in the ITCZ during the summer monsoon over Africa. Figure 5 (bottom) shows as an illustration the PC1 and PC2 time series in summer 1979. This depicts a similar contribution of these two components with high weights in August and September. These components are in temporal quadrature and have a periodicity around 15 days. We will see in the following that this is associated with a westward-propagating signal, confirming the identification of ER waves at this periodicity within the African monsoon.

2) THE COMPOSITE FIELDS OVER AFRICA

To evaluate the impact of this ER mode on the total OLR and atmospheric circulation fields, we have used the same composite approach as for the 30–100-day ER signal. Figure 6 presents the time sequence of strong minus weak convective events for June–September 1979–2006 based on the reconstructed 10–30-day filtered ER OLR ITCZ index by S-EOF12, in terms of unfiltered OLR values and 700-hPa geopotential heights. This sequence goes from $t_0 - 12$ to $t_0 + 10$ days with a 2-day lag where t_0 is the reference day for the selected cases as in Fig. 5. This is based on a composite set of 117 (118) days for strong (weak) events occurrences (Table 3). The unfiltered OLR data are represented in terms of the Student's t-test values (with a value of 2 representing a significance level at 95%, and a value of 3 a significance level higher than 99%; raw data are shown in Fig. 7a at t_0). We have chosen to present this information only for the OLR patterns, in order to evaluate the significant impact of these atmospheric circulations on convection, and to keep the whole circulation organization fully observable. Wind and geopotential heights at 700 hPa have been also chosen because the patterns are clearer than nearer the surface, with the 925-hPa fields similar but a bit noisier (not shown).

The composite time sequence of the ER signal (Fig. 6) displays a westward propagation of OLR anomalies along the mean latitude of the ITCZ between 10° and 15°N, resulting in a modulation of convective activity within the ITCZ without any significant changes in its latitudinal location. The apparent wavelength is about 70°–80° of longitude and the period is close to 15 days (also estimated from the composite time series of the

Unauthenticated | Downloaded 11/02/21 07:41 PM UTC

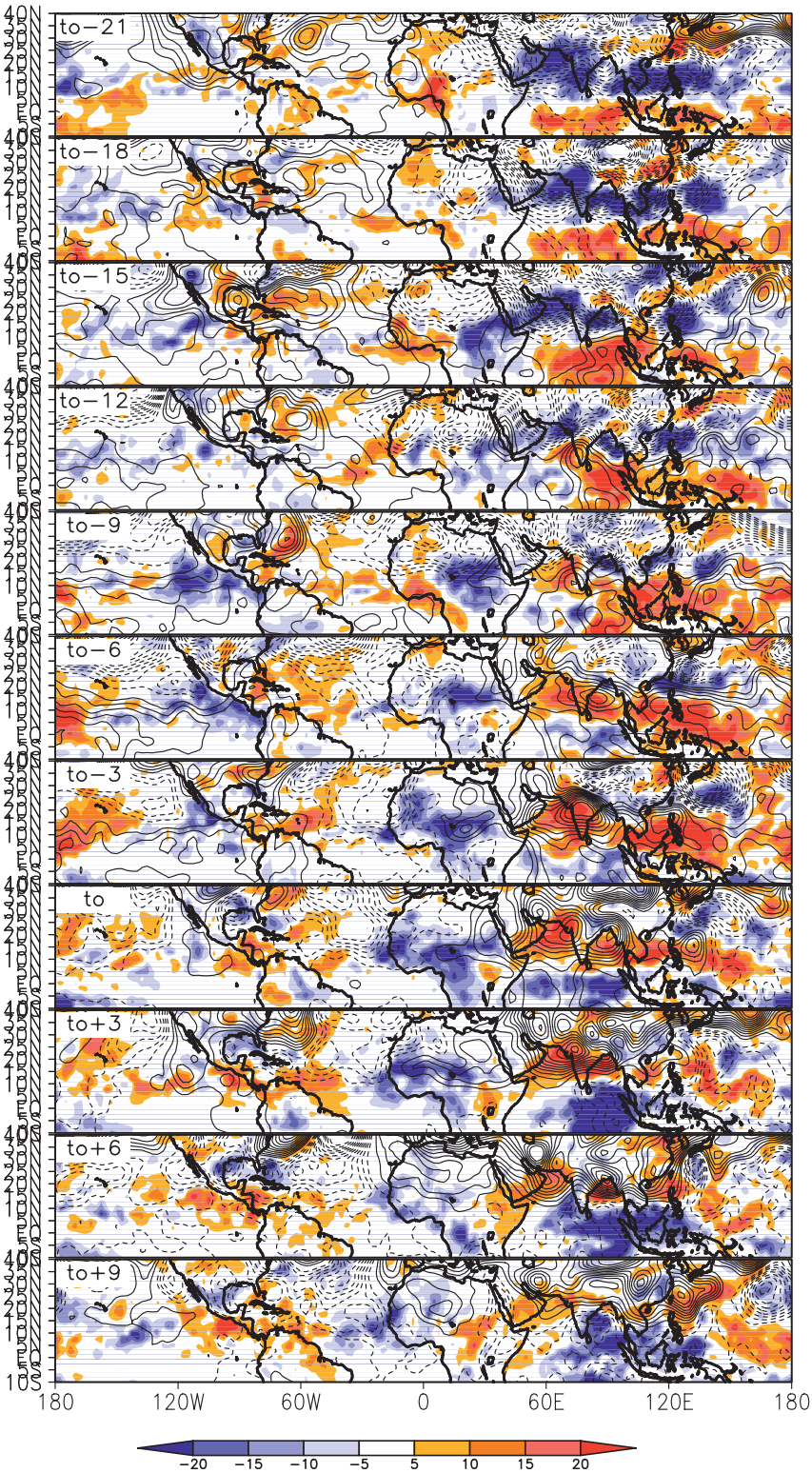

FIG. 4. Time sequence of strong minus weak convective events for June–September 1979–2006 based on the reconstructed 30–100-day filtered ER OLR ITCZ index by S-EOF1 and S-EOF2 (called S-EOF12): unfiltered OLR values (colors; W m^{-2}) and 925-hPa geopotential heights [solid (dashed) contours for positive (negative) values; isolines are drawn every 2 gpm with the zero isoline omitted]. (top to bottom) Time $t_0 - 21$ to $t_0 + 9$ days with a time lag of 3 days.

Unauthenticated | Downloaded 11/02/21 07:41 PM UTC

TABLE 4. Percentages of explained variance of the S-EOF of the 10–30-day filtered ER signal.

Eigenvalue	Variance (%)	Cumulated variance (%)
1	15.5	15.5
2	13.7	29.2
3	7.8	37.0
4	7.2	44.2
5	5.6	49.8
6	4.9	54.7

reconstructed ITCZ OLR index over 7.5°–12.5°N, 10°W–10°E; not shown), giving an approximate phase speed of 6 m s^{-1}. This signal induces highly significant OLR modulations greater than 10 W m^{-2} and rainfall variations in excess of 2 mm day^{-1} (see at t_0 on Figs. 7a,b). The initiation of the signal can be seen at $t_0 - 10$ located near Lake Victoria to 25°N. Only the northern part (north of 10°N) persists and subsequently moves westward. When the OLR signal reaches the western coast of West Africa, it becomes more extended meridionally from the equator to 30°N. Then, its amplitude decreases rather rapidly as it crosses into the tropical Atlantic.

This OLR pattern is associated with wind and geopotential fields at 700 hPa. At t_0, north of 7.5°N, there is an alternation of anticyclonic (40°W), cyclonic (10°W), and anticyclonic (20°E) cells from west to east, associated with weaker cells of the opposite sign south of 7.5°N (around 35°W, 10°W, and 30°E, respectively). These circulations are consistent with OLR anomalies, with the cyclonic cells located ahead of the negative OLR anomalies advecting moisture and causing wave-induced convergence within the enhanced convective area, and vice versa. Similar circulation anomalies are present at 925 hPa (not shown), enhancing the Saharan depression from $t_0 - 4$ to t_0 and weakening it from $t_0 + 4$ to $t_0 + 8$. OLR anomalies of the same sign occur at the same longitudes both at 15°N and at the equator.

This pattern looks like a theoretical ER wave solution on an equatorial β plane (Matsuno 1966). Different interpretations can be suggested. First, it looks like an $n = 1$ ER wave with meridional wavenumber of one (see Fig. 3 of Yang et al. 2003), but displaced north of the equator, around 7.5°N, with a more developed signal north of 7.5°N than south of 7.5°N. This could be due to the monsoon background state because Zhang and Webster (1989) have demonstrated that changes in the structures resulting from the non–Doppler effect of the basic state can be considerable for the ER wave. Second, it may also be interpreted as an $n = 2$ ER wave solution (see again Fig. 3 of Yang et al. 2003). Finally, as suggested by Yang et al. in their more general study (Yang et al. 2007, p. 3444), the best interpretation may be a combination of $n = 1$ and $n = 2$ Rossby solutions. This interpretation has the advantage of producing an asymmetric wind field with a stronger signal north of the equator and a weaker one to the south, as is seen at t_0 in Fig. 6.

The OLR initiation of this ER wave pattern, located at $t_0 - 10$ over eastern Africa, is initially more developed to the south (just north of Lake Victoria). In the following days, however, only the northern part of the OLR signal amplifies and propagates westward. This could be due to the fact that east of 10°E the ITCZ is more extended southward over the African landmass while west of 10°E it extends to the north of the Guinea Gulf because of the cold sea surface temperatures present there. The OLR anomaly pattern is very consistent with the divergent wind field at 200 (Fig. 7a) and 850 (Fig. 7b) hPa, as well as the GPCP rainfall field. This consists of opposite divergent wind fields in the lower and upper troposphere, suggesting a vertical structure forced as the peak projection response to the deep convective heating.

A possible connection with the Indian monsoon system is also suggested by the 700-hPa circulation. At $t_0 - 4$, for instance, the three centers of the ER circulation signal are located at 60°E, 10°E, and 30°W and are associated with positive, negative, and positive OLR anomaly poles, respectively. Further analysis of this issue is, however, beyond the scope of the paper.

b. *The 10–30-day Sahel mode*

1) THE S-EOF PATTERNS

To examine the Sahel mode in this section, an S-EOF analysis has been performed on 10–30-day filtered OLR over West and central Africa during summer. A similar analysis was carried out by Mounier and Janicot (2004) using slightly different filtered data, but the conclusions remain similar. Following the Scree test, only the four first PCs can be retained. PC1, PC2, and PC3 are resolved with PC3 and PC4 forming a degenerate multiplet following the North et al. (1982) test. The main mode of convective variability seen through the first component (representing 10.2% of explained 10–30-day filtered variance; Table 5) has been identified as the QBZD mode (Mounier et al. 2008; see the introduction). EOF2 (8.5% of explained variance; Table 5) and EOF3/EOF4 (5.9% and 5.3% of explained variance, respectively; Table 5) have been combined to characterize the second primary mode of convection over West and central Africa, as was done in Mounier and Janicot (2004). Figure 8 (top) shows the EOF2, EOF3, and EOF4 patterns. The EOF2 pattern depicts a zonal dipole along the Sahelian latitudes between 10° and 15°N with a northeast and a southeast extension for the leading positive pole. The EOF3 pattern shows a westward displacement of the EOF2 pattern (confirmed in the next section), and

Unauthenticated | Downloaded 11/02/21 07:41 PM UTC

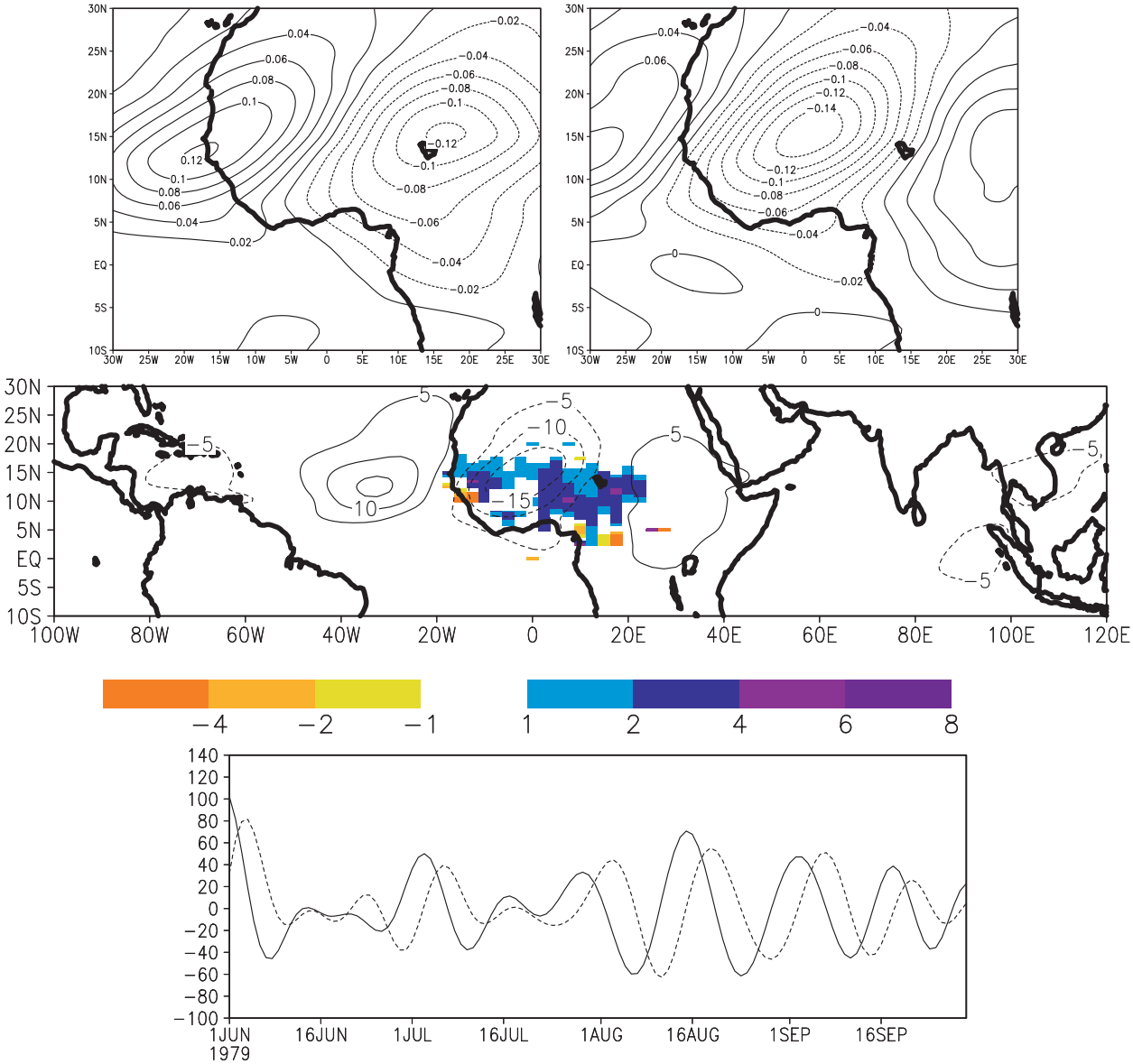

FIG. 5. As in Fig. 3, but for the 10–30-day filtered ER OLR signal.

a positive pole centered over central Africa. EOF4 has a more complex pattern in quadrature with the EOF3 pattern. The associated PC2 and PC3 time series are in temporal quadrature with a peak correlation of +0.4 significant at the 0.001 level for a lag of 4 days, so that these two components represent a propagating signal of convection.

Figure 8 (bottom) displays the associated composite field of 10–30-day filtered OLR (contours) for the difference between strong and weak convective phases based on the combination of EOF2, EOF3, and EOF4. This has been computed by reconstructing filtered OLR values over the ITCZ area of 7.5°–12.5°N, 10°W–10°E, as in Fig. 3. The strong cases have been selected when the standardized reconstructed ITCZ index is at a minimum and greater than −1, and the reverse for the weak cases. Similar composite fields for unfiltered rainfall data are also displayed (color). The OLR pattern is very similar to the Sahel mode identified by Sultan et al. (2003) using as a reference a regional index of filtered rainfall over the area of 12.5°–15°N, 10°W–10°E. This pattern depicts two opposite poles of OLR anomalies: one ahead centered around 15°N and covering all of West Africa with a northeastward extension, and another centered over equatorial Africa covering the domain from 5°S to 15°N. On average, 4.5 strong and 4.3 weak events occur per

Unauthenticated | Downloaded 11/02/21 07:41 PM UTC

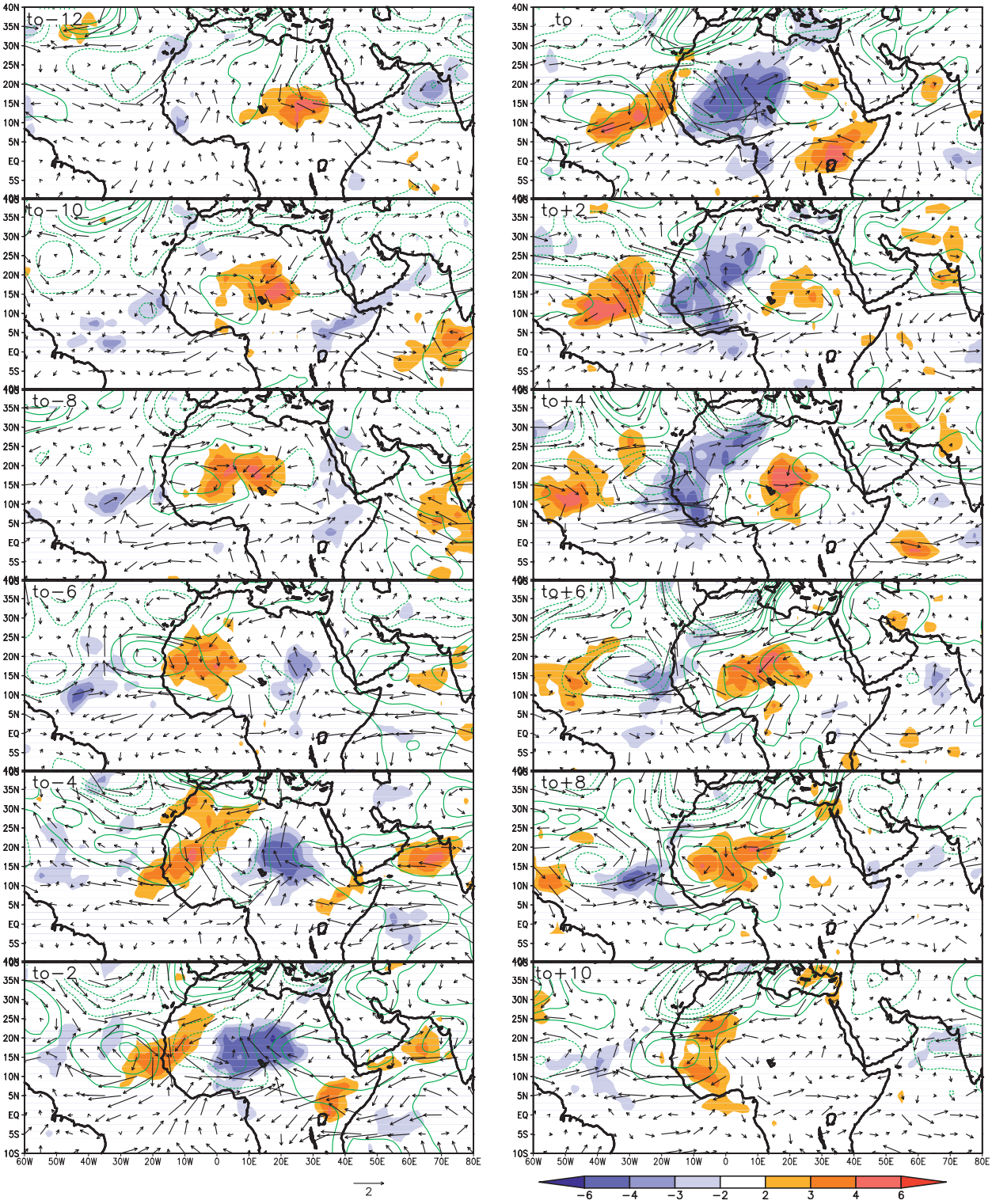

FIG. 6. As in Fig. 4, but based on the reconstructed 10–30-day filtered ER OLR ITCZ index: unfiltered OLR values (colors; values are expressed in terms of Student's t test), 700-hPa wind vectors (m s^{-1}), and 700-hPa geopotential heights [green solid (dashed) contours for positive (negative) values; isolines are drawn every 2 gpm with the zero isoline omitted]. For clarity, only one grid point out of two is represented for the wind vectors. (top to bottom) Time $t_0 - 12$ to $t_0 + 10$ days with a time lag of 2 days.

Unauthenticated | Downloaded 11/02/21 07:41 PM UTC

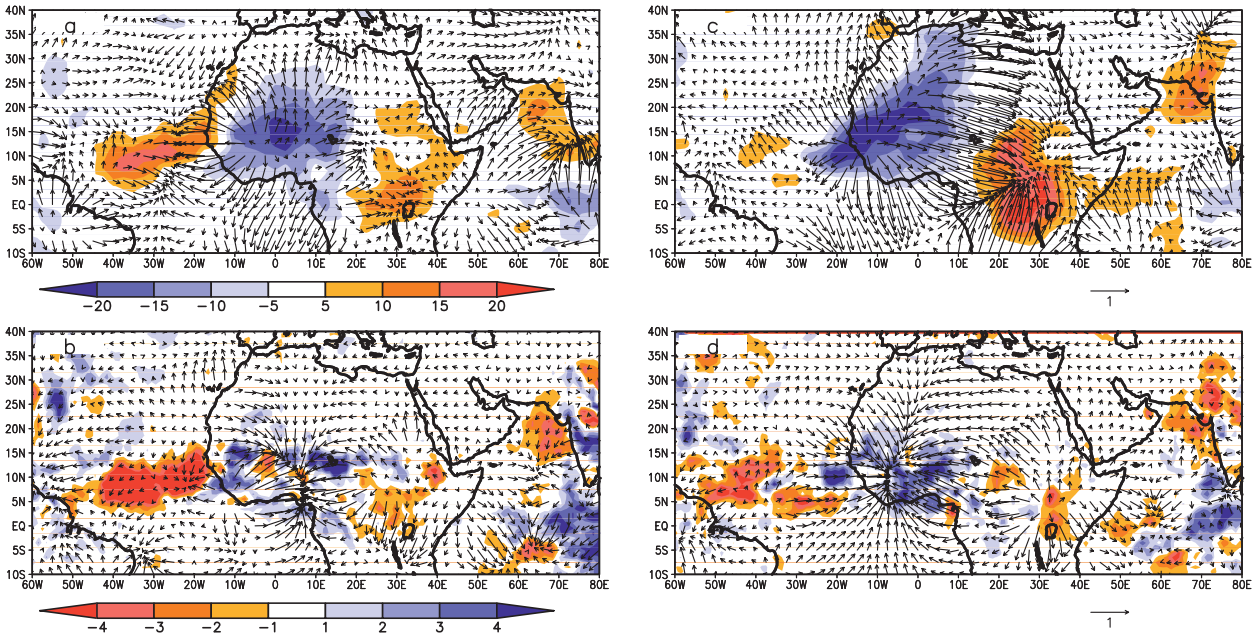

FIG. 7. (a) Strong minus weak convective events at t_0 for June–September 1979–2006 based on the reconstructed 10–30-day filtered ER OLR ITCZ index by S-EOF1 and S-EOF2: unfiltered OLR values (colors; units: W m^{-2}), and 200-hPa divergent wind vectors (m s^{-1}). (b) As in (a), but for the unfiltered GPCP values over the period 1997–2006 (colors; mm day^{-1}) and 700-hPa divergent wind vectors (m s^{-1}). (c) As in (a), but for the reconstructed 10–30-day filtered OLR ITCZ index by S-EOF2, S-EOF3, and S-EOF4. (d) As in (b), for the reconstructed 10–30-day filtered OLR ITCZ index by S-EOF2, S-EOF3, and S-EOF4. Color scale is the same for (a) and (c), and for (b) and (d). Vector scale is the same for all the panels.

summer (Table 3). The rainfall anomaly pattern is consistent with the OLR pattern, with positive values west of 15°E covering the ITCZ location and negative anomalies between 15° and 20°E (no data are available east of 20°E). However, the positive rainfall anomalies extend more eastward than the negative OLR anomalies. This discrepancy can be partly explained by the fact that we compare filtered with unfiltered data. Figure 7c shows the corresponding composite unfiltered OLR field and Fig. 7d the corresponding composite unfiltered GPCP field. The negative OLR values extend more to the east than the filtered ones (the -5 W m^{-2} isoline is located west of Lake Chad for filtered data and reaches Lake Chad for the unfiltered data), as with the unfiltered positive GPCP and IRD rainfall values. The high range of these OLR and rainfall differences between the strong and weak phases confirms that this mode is able to significantly modulate the convective activity in the ITCZ during the summer monsoon over the whole of sub-Saharan Africa.

2) THE COMPOSITE FIELDS OVER AFRICA

Figure 9 presents a similar time sequence of strong minus weak convective events for June–September 1979–2006, but based on the reconstructed 10–30-day filtered OLR ITCZ index by S-EOF234, in terms of unfiltered OLR values and 700-hPa geopotential heights. This is based on a composite set of 121 (125) days for strong (weak) events occurrences (Table 3). This composite time sequence is similar to the signal previously detected by Sultan et al. (2003). The OLR signal initiates over eastern equatorial Africa (see $t_0 - 12$ and $t_0 - 10$), enhances in situ ($t_0 - 8$), and then moves northward to 15°N ($t_0 - 6$), and finally propagates westward until dissipating over the tropical Atlantic ($t_0 + 4$). The apparent periodicity of this mode is approximately 15 days (also estimated from the composite time series of the reconstructed ITCZ OLR index over 7.5°–12.5°N, 10°W–10°E; not shown) and its wavelength is about 70° of longitude.

The atmospheric circulation structure at 700 hPa (also at 925 hPa; not shown) is very consistent with the OLR anomaly patterns with cyclonic circulation located ahead of negative OLR anomalies bringing more moisture into

TABLE 5. Percentages of explained variance of the S-EOF of the 10–30-day filtered signal.

Eigenvalue	Variance (%)	Cumulated variance (%)
1	10.2	10.2
2	8.5	18.7
3	5.9	24.6
4	5.3	29.9
5	3.9	33.8
6	3.8	37.6

Unauthenticated | Downloaded 11/02/21 07:41 PM UTC

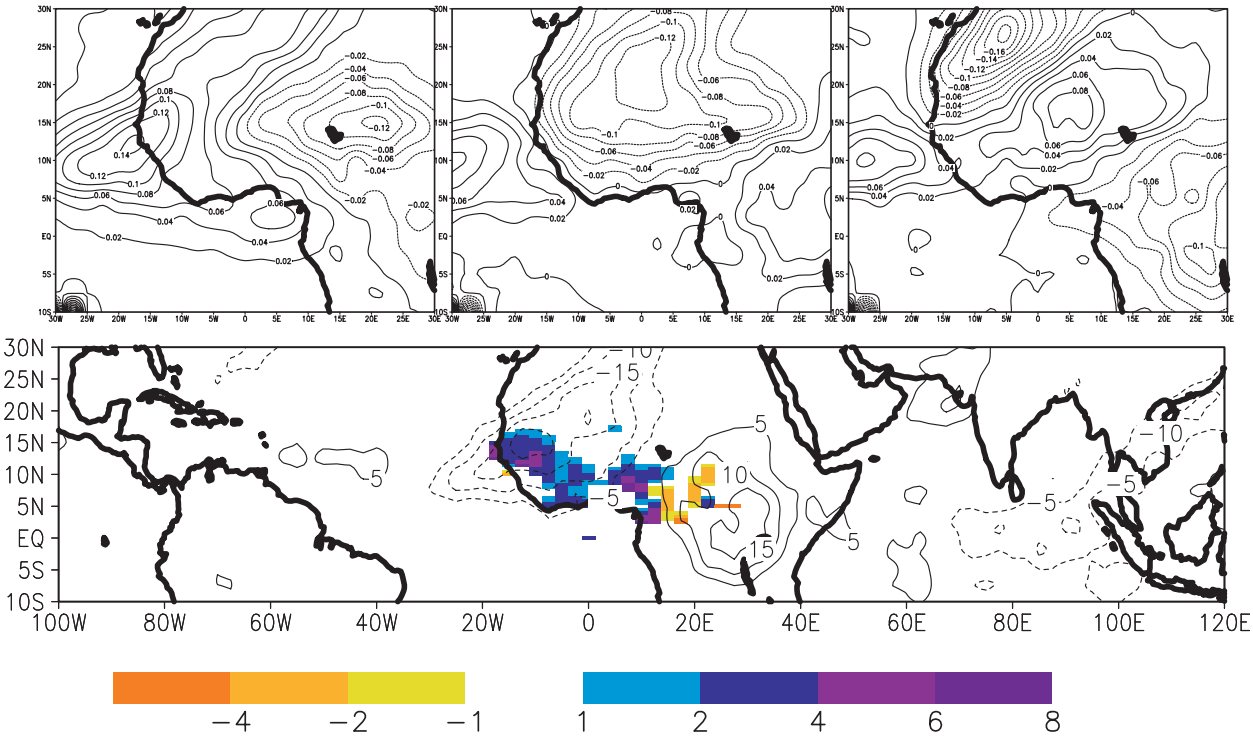

FIG. 8. (top) June–September 1979–2006 second, third, and fourth eigenvectors of the S-EOF analysis of the 10–30-day filtered OLR signal over West and central Africa. (bottom) Composite fields of the filtered 10–30-day OLR (contours) for the difference between strong and weak convective phase, computed by using the reconstruction of the OLR values over the ITCZ area 7.5°–12.5°N, 10°W–10°E by S-EOF2, S-EOF3, and S-EOF4 (S-EOF234). The strong (weak) cases have been selected when the standardized reconstructed OLR ITCZ index is minimum (maximum) and weaker (higher) than −1 (+1). Similar composite fields for unfiltered rainfall data but over the period 1979–90 (colors). OLR difference in W m^{-2} and rainfall difference in mm day^{-1}.

the enhanced convective area, and vice versa. As for the ER mode, the apparent northward propagation of the OLR anomaly pole east of 20°E from the equator to 15°–20°N could be due to the fact that east of 10°E the ITCZ is more extended southward over the African landmass, while west of 10°E the ITCZ is located north of the Guinea Gulf. Moreover, at $t_0 - 8$ and $t_0 - 6$, the low-level cyclonic cell moving westward along the Sahelian latitudes induces stronger southerly winds as well as a higher moisture content (not shown) east of 15°E and north of the negative OLR anomaly pole. This provides favorable conditions for increased convection there and for the observed northward displacement of the convective envelop. On the other hand, in the opposite phase from $t_0 - 4$ to $t_0 + 2$, the westward evolution of the Sahel mode structure described above induces the development of an anticyclonic cell east of 10°E, which brings drier air over equatorial Africa by northerly winds, a favorable condition for a decreased convection there and for the observed northward development of positive OLR anomalies.

The divergent wind patterns at 200 (Fig. 7c) and 850 (Fig. 7d) hPa are very well marked and associated with coherent OLR and GPCP anomaly patterns, with a strong baroclinic vertical structure. At t_0 the southwest–northeast divergent area extending from the Fouta–Djalon zone to the Mediterranean zone is associated with high negative OLR anomalies and northward moisture transport at the lower levels, inducing more convection and precipitation in the ITCZ and more humid and cloudy air, but without significant precipitation north of the ITCZ as seen in the GPCP field. The high-level divergent area appears to be linked to two subsiding areas, the main one associated with high positive OLR anomalies located over central and eastern Africa extending from the Congo basin to the Red Sea, and a weaker one south of the equator over the Atlantic.

c. *Comparison between the ER and the Sahel modes*

The Sahel mode patterns of atmospheric circulation and convection are very similar to the ER signal patterns, with similar periodicity, wavelength, spatial patterns of OLR and atmospheric circulation, and similar axes of propagation. This suggests that the Sahel mode could be accounted for in part by ER wave occurrences. Over the summers of 1979–2006 the correlation coefficient between

Unauthenticated | Downloaded 11/02/21 07:41 PM UTC

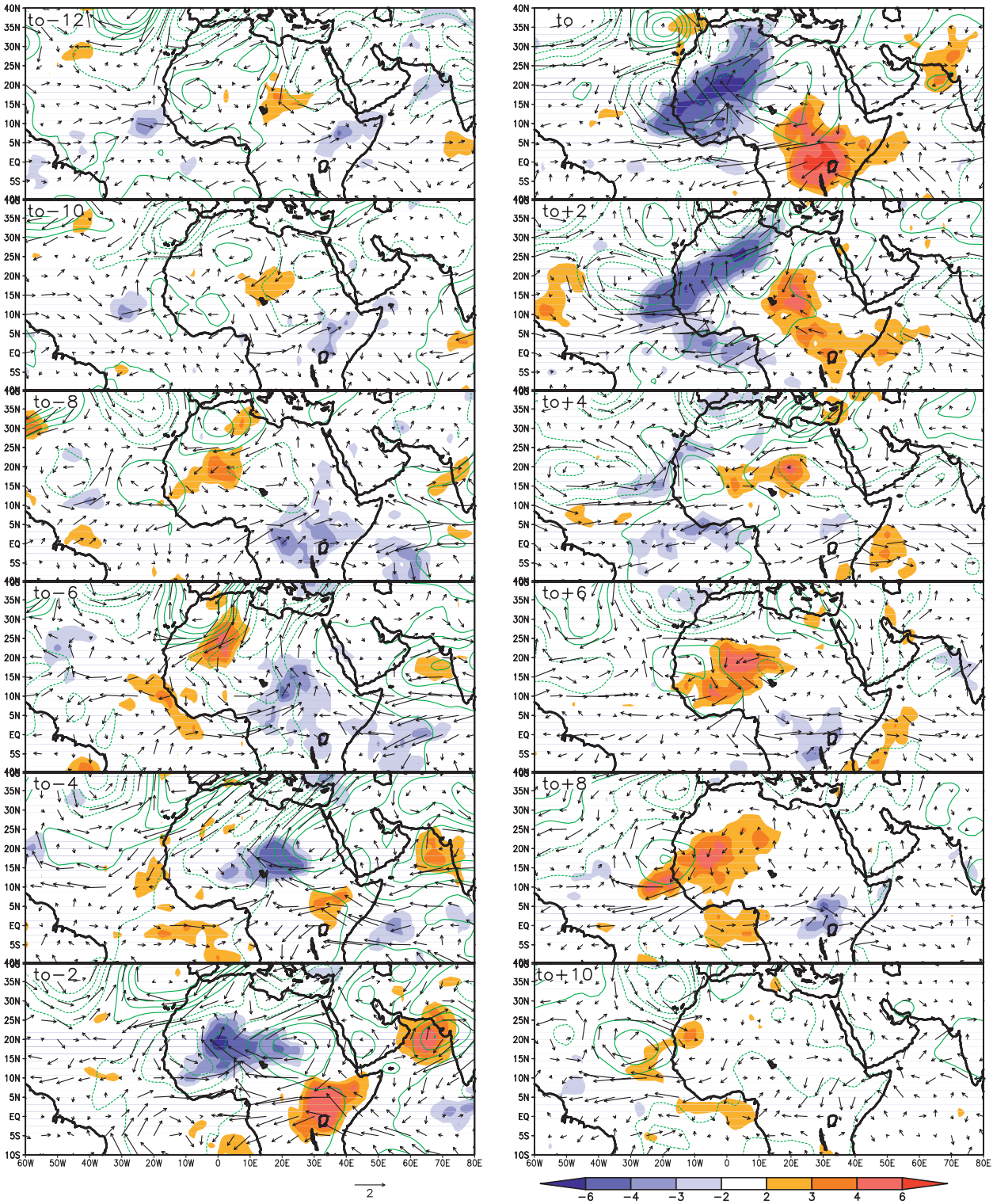

FIG. 9. As in Fig. 6, but filtered index by S-EOF2, S-EOF3 and S-EOF4 (S-EOF234).

Unauthenticated | Downloaded 11/02/21 07:41 PM UTC

the time sequences of the reconstruction of the ITCZ OLR index by the ER and Sahel mode signals is equal to +0.5 at zero lag and +0.62 with a 2-day lag (the Sahel mode being ahead of the ER signal). This means that there are sequences where these two signals are highly coincident and other times when they are uncorrelated (not shown). This lag between the two signals, which is detectable when comparing Figs. 7a and 7c, for instance, can been explained by the occurrence for the Sahel mode of a 1-day lag between the filtered and the unfiltered ITCZ OLR index computed on 7.5°–12.5°N, 10°W–10°E, whereas for the ER signal the corresponding indexes have no lag between them. When the filtered Sahel mode index is at its maximum, the corresponding unfiltered OLR pattern is not centered on 10°W–10°E but is already located a bit westward.

The Sahel mode and ER patterns also display certain differences. Indeed, in Figs. 6 and 9 the Sahel mode displays a pattern in which the northern part of the circulation more developed than the observed ER one. From $t_0 - 8$, the cyclonic cell at 15°–20°E, amplifying and moving westward, is more developed for the Sahel mode than for the ER signal, and contributes to an enhanced negative OLR anomaly pattern located first over equatorial Africa and then over West Africa. From $t_0 - 4$, the trailing anticyclonic cell located at 30°E is also strengthening more for the Sahel mode, inducing in the subsequent days a higher positive OLR anomaly pattern first over equatorial Africa and then over West Africa. This enhanced OLR signal over equatorial Africa leads to an apparent northward propagation of the OLR anomaly pattern east of 20°E for the Sahel mode, while this is less clear for the ER signal.

Figure 10 displays the $t_0 - 12$ to $t_0 + 8$ sequence of composite of strong minus weak convective events for different combinations of the Sahel mode and ER signals. The ''pure'' Sahel mode is represented on the left column by considering only Sahel mode cases when the absolute value of the standardized ER index is lower than 1 (this represents the average of 82 strong events minus 74 weak events). The occurrence of the Sahel mode with a high ER signal is represented in the middle column by considering only cases when the absolute value of the standardized ER index is higher than 1 (representing 43 strong events and 46 weak events). Finally the ''pure'' ER signal is represented on the right column by considering only ER cases when the absolute value of the standardized Sahel mode index is lower than 1 (representing 69 strong events and 69 weak events). The significance of the OLR anomalies is expressed in terms of the Student's *t*-test values as for Figs. 6 and 9. These sample numbers indicate that in approximately one-third of the ER and Sahel mode cases are combined while in two-thirds of the cases they are independent. The panels of Fig. 10 confirm that the main difference between the ''pure'' Sahel mode and ER signal is the occurrence of a strong OLR anomaly pole over equatorial Africa when the Sahel mode is well developed. Once it is located more to the west, its patterns looks more like the ER signal. However, at this stage we note another difference: the Sahel mode depicts a meridional dipole of convection (see $t_0 - 4$ or $t_0 + 4$) over West Africa while the ER signal has one-sign pole of OLR anomalies, meaning that the ITCZ will be displaced meridionally with the Sahel mode and not with the ER mode. When the Sahel mode is associated with a strong ER signal (middle column), the northern part of the OLR anomaly patterns is enhanced and the southern part is weakened, providing a more symmetric pattern east of 20°E.

6. Conclusions and synthesis of intraseasonal variability in the summer African monsoon

Two kinds of convectively coupled ER waves have been detected within the summer African monsoon in this study. We have focused on the main signal of convection by retaining the leading EOF modes of OLR variability. Within the periodicity band 30–100 days, an ER wave pattern with an approximate wavelength of 13 500 km has been depicted. This ER wave links the MJO variability mode in the Indian monsoon sector with the main mode of convective variability over West and central Africa detected by Matthews (2004). This result confirms the investigation carried out in Janicot et al. (2009) and Lavender and Matthews (2009).

Within the 10–30-day periodicity band, an ER wave pattern has been highlighted in the African monsoon system with an approximate wavelength of 7500 km, a westward phase speed of 6 m s^{-1}, and a period of 15 days. This signal looks like a combination of $n = 1$ and $n = 2$ ER solutions. Its vertical first baroclinic profile suggests that this wave is forced by the deep convective heating. Its OLR signal is initially detected north of Lake Victoria, and then this signal expands northward and propagates westward along the Sahel latitudes.

In the same 10–30-day periodicity band the Sahel mode, identified first by Sultan et al. (2003) and corresponding to the second main mode of convective variability within the 10–30-day periodicity band (Mounier and Janicot 2004), has also been examined in detail here. The main difference between these two statistical results is that the Sahel mode comes from a larger spectral domain than the ER mode, and includes both eastward and westward propagation along with symmetric and antisymmetric components about the equator. We have obtained a high spatial similarity between the ER and the Sahel modes, a significant correlation in time (+0.6), and

Unauthenticated | Downloaded 11/02/21 07:41 PM UTC

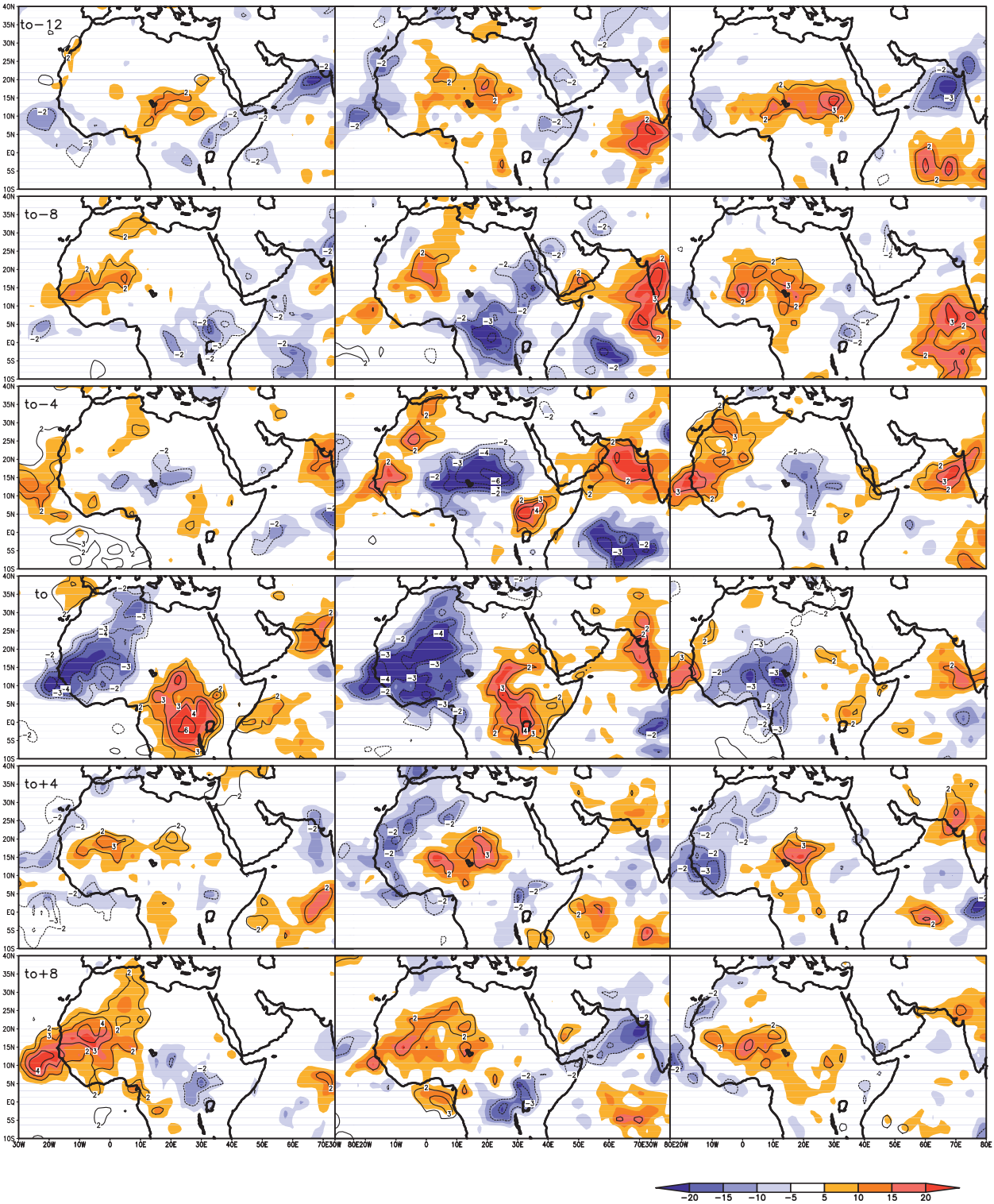

FIG. 10. Time sequence from $t_0 - 12$ to $t_0 + 8$ days with a time lag of 4 days of composite strong minus weak convective events for June–September 1979–2006 based on different reconstruction of 10–30-day filtered OLR signals. (left) Unfiltered OLR for days when the standardized Sahel mode signal is >1 in absolute value and the standardized ER signal is <1; (middle) unfiltered OLR for days when the standardized Sahel mode signal is >1 in absolute value and the standardized ER signal is >1; and (right) unfiltered OLR for days when the standardized ER signal is >1 in absolute value and the standardized Sahel mode signal is <1. OLR values are in colors (W m^{-2}) and the same OLR values are expressed in terms of Student's t test are in contours.

Unauthenticated | Downloaded 11/02/21 07:41 PM UTC

similar westward propagation, so we conclude that the ER wave (or at least its dominant EOF mode) can support the Sahel mode dynamics. This provides support to notion of a ''purely internal atmospheric mode'' proposed by Lavender et al. (2010) to explain Sahel mode dynamics, in addition to soil moisture and land surface interactions. However, this explanation is not complete; the correlation explains about 36% of the common variance, so only about one-third of Sahel mode events are concomitant with an ER wave occurrence. In addition, the Sahel mode pattern has higher weights over the eastern and central Africa. This means that supplementary physical processes must be involved in Sahel mode dynamics, which need to be investigated further.

This paper is the last in a series of studies documenting the West African summer monsoon variability at intraseasonal time scales (Sultan et al. 2003; Sultan and Janicot 2003; Mounier and Janicot 2004; Mounier et al. 2007, 2008; Janicot et al. 2009). This is a critical time scale in this region where resources are strongly rainfall dependent, so the basic mechanisms controlling this variability as well as its predictability must be investigated. Three main modes have been highlighted in these studies, the ''QBZD'' and the ''Sahel'' modes, with a mean periodicity around 15 days, and the ''MJO'' mode, with a mean periodicity around 40 days. These modes have a regional extension and are manifested by convective envelopes modulating the activity of a population of individual, higher-frequency systems. They are intermittent (about 5.5 strong–weak QBZD mode events, 4.5 strong–weak Sahel mode events, and 1.5 strong–weak MJO events in an average June–September period), but their impact on precipitation and convective activity is strong when they occur. They are characterized by marked zonal propagation, which is westward for the MJO and Sahel modes and eastward for the QBZD mode, with an important stationary component for the latter over Africa. These modes appear to be mainly controlled both by internal atmospheric dynamics (convectively coupled equatorial Rossby waves for the MJO and Sahel modes, and equatorial Kelvin waves for the QBZD mode) and by land surface interactions (Taylor 2008). More investigation of these issues is however needed. For instance, internal atmospheric processes, like transient mean flow interactions between the African easterly jet and the African easterly waves, can produce convective fluctuations at the intraseasonal time scale (Cornforth et al. 2009; Leroux et al. 2009). These modes are also a source and a part of some teleconnection mechanisms, especially between the African and Indian monsoon sectors, but also between the extratropics and the Mediterranean sector, as shown in recent studies (Vizy and Cook 2009; Chauvin et al. 2010). They can also have an impact on the specific timing of the African monsoon onset, which is characterized by a northward abrupt shift of the ITCZ occurring at the end of June or the beginning of July, depending of the year. Some possible mechanisms for the African monsoon onset have been identified, such as the link with the oceanic cold tongue establishment in the Guinea Gulf (G. Caniaux et al. 2009, personal communication), or the Saharan heat low dynamics during its establishment over the northwestern part of Africa (Sultan and Janicot 2003; Ramel et al. 2006; Lavaysse et al. 2009), as well as its role in inertial instability release (Hagos and Cook 2007). However, it has also been shown that intraseasonal events like the African MJO mode could have a role in the African monsoon onset in 2006 during the African Monsoon Multidisciplinary Analysis (AMMA) intensive field campaign (Janicot et al. 2008). These intraseasonal modes also probably have a strong impact during the other seasons of the year when the ITCZ is located close to or over the equator, and when equatorial atmospheric dynamics and its interaction with convection should be stronger. Finally, preliminary work has shown that some predictability skill exists at this intraseasonal time scale (Sultan et al. 2009). A better knowledge of the mechanisms controlling this scale is necessary to improve this skill and to be able to provide guidance for the benefit of farmers and stakeholders over West Africa.

Acknowledgments. We are thankful to NOAA-CIRES Climate Diagnostics Center (Boulder, CO) for providing the NCEP–NCAR reanalysis dataset and the interpolated OLR dataset from their Web site (online at http://www.cdc.noaa.gov/). The authors also thank the reviewers for helping to clarify the text. Based on French initiative, AMMA was built by an international scientific group and is currently funded by a large number of agencies, especially from France, the United Kindgom, the United States, and Africa. It has been the beneficiary of a major financial contribution from the European Community's Sixth Framework Research Programme. Detailed information on scientific coordination and funding is available on the AMMA International Web site (http://www.amma-international.org).

REFERENCES

Cattell, R. B., 1966: The scree test for the number of factors. *Multivariate Behav. Res.,* **1,** 245–276.

Chauvin, F., R. Roehrig, and J.-P. Lafore, 2010: Intraseasonal variability of the Saharan heat low and its link with midlatitudes. *J. Climate,* **23,** 2544–2561.

Cornforth, R., C. Thorncroft, and B. Hoskins, 2009: The impact of moist processes on the African easterly jet–African easterly wave system. *Quart. J. Roy. Meteor. Soc.,* **135,** 894–913.

Unauthenticated | Downloaded 11/02/21 07:41 PM UTC

Ghil, M., and Coauthors, 2002: Advanced spectral methods for climatic series. *Rev. Geophys.,* **40,** 1003, doi:10.1029/2000RG000092.

Grueber, A., and A. F. Krueger, 1974: The status of the NOAA outgoing longwave radiation data set. *Bull. Amer. Meteor. Soc.,* **65,** 958–962.

Hagos, S. M., and K. H. Cook, 2007: Dynamics of the West African monsoon jump. *J. Climate,* **20,** 5264–5284.

Huffman, G. J., R. F. Adler, M. M. Morrissey, D. T. Bolvin, S. Curtis, R. Joyce, B. McGavock, and J. Susskind, 2001: Global precipitation at one-degree daily resolution from multisatellite observations. *J. Hydrometeor.,* **2,** 36–50.

Janicot, S., and B. Sultan, 2001: Intra-seasonal modulation of convection in the West African monsoon. *Geophys. Res. Lett.,* **28,** 523–526.

——, and Coauthors, 2008: Large scale overview of the summer monsoon over the summer monsoon in West Africa during the AMMA field experiment in 2006. *Ann. Geophys.,* **26,** 2569–2595.

——, F. Mounier, N. M. Hall, S. Leroux, B. Sultan, and G. Kiladis, 2009: The dynamics of the West African monsoon. Part IV: Analysis of 25–90-day variability of convection and the role of the Indian monsoon. *J. Climate,* **22,** 1541–1565.

Kalnay, E., and Coauthors, 1996: The NCEP/NCAR 40-Year Reanalysis Project. *Bull. Amer. Meteor. Soc.,* **77,** 437–471.

Kanamitsu, M., W. Ebisuzaki, J. Woollen, S.-K. Yarg, J. J. Hnilo, M. Fiorino, and G. L. Potter, 2002: NCEP/DOE AMIP-II Reanalysis (R-2). *Bull. Amer. Meteor. Soc.,* **83,** 1631–1643.

Kiladis, G. N., C. D. Thorncroft, and N. M. J. Hall, 2006: Three dimensional structure and dynamics of African easterly waves. Part I: Observations. *J. Atmos. Sci.,* **63,** 2212–2230.

——, M. C. Wheeler, P. T. Haertel, K. H. Straub, and P. E. Roundy, 2009: Convectively coupled equatorial waves. *Rev. Geophys.,* **47,** RG2003, doi:10.1029/2008RG000266.

Lavaysse, C., C. Flamant, S. Janicot, D.-J. Parker, J.-P. Lafore, B. Sultan, and J. Pelon, 2009: Seasonal cycle of the West African heat low: A climatological perspective. *Climate Dyn.,* **33,** 313–330, doi:10.1007/s00382-009-0553-4.

Lavender, S. L., and A. J. Matthews, 2009: Response of the West African monsoon to the Madden–Julian oscillation. *J. Climate,* **22,** 4097–4116.

——, C. M. Taylor, and A. J. Matthews, 2010: Coupled land–atmosphere intraseasonal variability of the West African monsoon in a GCM. *J. Climate,* in press.

Leroux, S., N. M. J. Hall, and G. N. Kiladis, 2009: A climatological study of transient-mean-flow interactions over West Africa. *Quart. J. Roy. Meteor. Soc.,* **136,** 397–410.

Liebmann, B., and C. A. Smith, 1996: Description of a complete (interpolated) outgoing longwave radiation dataset. *Bull. Amer. Meteor. Soc.,* **77,** 1275–1277.

Madden, R. A., and P. R. Julian, 1994: Observations of the 40–50-day tropical oscillation. *Mon. Wea. Rev.,* **122,** 814–837.

Maloney, E. D., and J. Shaman, 2008: Intraseasonal variability of the West African monsoon and Atlantic ITCZ. *J. Climate,* **21,** 2898–2918.

Matsuno, T., 1966: Quasi-geostrosphic motion in the equatorial area. *J. Meteor. Soc. Japan,* **44,** 25–42.

Matthews, A. J., 2004: Intraseasonal variability over tropical Africa during northern summer. *J. Climate,* **17,** 2427–2440.

Mounier, F., and S. Janicot, 2004: Evidence of two independent modes of convection at intraseasonal timescale in the West African summer monsoon. *Geophys. Res. Lett.,* **31,** L16116, doi:10.1029/2004GL020665.

——, G. N. Kiladis, and S. Janicot, 2007: Analysis of the dominant mode of convectively coupled Kelvin waves in the West African monsoon. *J. Climate,* **20,** 1487–1503.

——, S. Janicot, and G. N. Kiladis, 2008: The West African monsoon dynamics. Part III: The quasi-biweekly zonal dipole. *J. Climate,* **21,** 1911–1928.

North, G. R., R. F. Bell, R. F. Cahalan, and F. J. Moeng, 1982: Sampling errors in the estimation of empirical orthogonal function. *Mon. Wea. Rev.,* **110,** 699–706.

Pohl, B., B. Fontaine, S. Janicot, and R. Marteau, 2009: Implication of the Madden–Julian oscillation in the 40-day variability of the West African monsoon, and associated rainfall anomalies. *J. Climate,* **22,** 3769–3785.

Ramel, R., H. Galle, and C. Messager, 2006: On the northward shift of the West African monsoon. *Climate Dyn.,* **26,** 429–440.

Richman, M. B., 1986: Rotation on principal component. *J. Climatol.,* **6,** 293–335.

Roundy, P. E., and W. M. Frank, 2004: A climatology of waves in the equatorial region. *J. Atmos. Sci.,* **61,** 2105–2132.

Straub, K. H., and G. N. Kiladis, 2002: Observations of convectively coupled Kelvin waves in the eastern Pacific ITCZ. *J. Atmos. Sci.,* **59,** 30–53.

Sultan, B., and S. Janicot, 2000: Abrupt shift of the ITCZ over West Africa and intra-seasonal variability. *Geophys. Res. Lett.,* **27,** 3353–3356.

——, and ——, 2003: The West African monsoon dynamics. Part II: The ''preonset'' and ''onset'' of the summer monsoon. *J. Climate,* **16,** 3389–3406.

——, ——, and A. Diedhiou, 2003: The West African monsoon dynamics. Part I: Documentation of intraseasonal variability. *J. Climate,* **16,** 3407–3427.

——, C. Baron, M. Dingkuhn, and S. Janicot, 2005: Agricultural impacts of large-scale variability of the West African monsoon. *Agric. For. Meteor.,* **128,** 93–110.

——, S. Correia, and S. Janicot, 2009: Medium-lead prediction of intraseasonal oscillations in West Africa. *Wea. Forecasting,* **24,** 767–784.

Taylor, C. M., 2008: Intraseasonal land–atmosphere coupling in the West African monsoon. *J. Climate,* **21,** 6636–6648.

Vautard, R., and M. Ghil, 1989: Singular spectrum analysis in nonlinear dynamics with applications to paleoclimatic time series. *Physica D,* **35,** 392–424.

——, P. Yiou, and M. Ghil, 1992: Singular spectral analysis: A toolkit for short, noisy chaotic signals. *Physica D,* **58,** 95–126.

Vizy, E. K., and K. H. Cook, 2009: A mechanism for African monsoon breaks: Mediterranean cold air surges. *J. Geophys. Res.,* **114,** D01104, doi:10.1029/2008JD010654.

Wheeler, M., and G. N. Kiladis, 1999: Convectively coupled equatorial waves: Analysis of clouds and temperature in the wavenumber–frequency domain. *J. Atmos. Sci.,* **56,** 374–399.

——, ——, and P. J. Webster, 2000: Large scale dynamical fields associated with convectively coupled equatorial waves. *J. Atmos. Sci.,* **57,** 613–640.

Yang, G.-Y., B. Hoskins, and J. Slingo, 2003: Convectively coupled equatorial waves: A new methodology for identifying wave structures in observational data. *J. Atmos. Sci.,* **60,** 1637–1654.

——, ——, and ——, 2007: Convectively coupled equatorial waves. Part III: Synthesis structures and their forcing and evolution. *J. Atmos. Sci.,* **64,** 3438–3451.

Zhang, C., and P. J. Webster, 1989: Effects of zonal flows on equatorially trapped waves. *J. Atmos. Sci.,* **46,** 3632–3652.

Unauthenticated | Downloaded 11/02/21 07:41 PM UTC